ORIGINAL PAPER

Study of Nd$_{2-x}$Ce$_x$CuO$_{4\pm\delta}$ (x=0.1–0.25) as cathode material for intermediate-temperature solid oxide fuel cells

Anushree Purushottam Khandale ·
Shyam Shashibhushan Bhoga

Abstract The solid solubility limit of Ce in Nd$_{2-x}$Ce$_x$CuO$_{4\pm\delta}$, prepared by sol–gel process, is established up to x=0.2. The transition from negative temperature coefficient to positive temperature coefficient, within the solid solubility region, is observed at 620 °C. The area-specific-resistance (ASR) is optimized for electrochemical cell sintered at 800 °C. ASR enhances with increase in sintering temperature of cell. ASR value of 0.93 ohm cm^2 at 700 °C, determined by electrochemical impedance spectroscopy is comparable against that by voltage versus current (V–I) characteristics at 0.98 ohm cm^2 at the same temperature. Electrochemical performance and ASR of Nd$_{1.8}$Ce$_{0.2}$CuO$_{4\pm\delta}$ is improved when prepared by sol–gel route over solid-state reaction, which is attributed to uniform size and shape of nanocrystalline grains.

Keywords Sol–gel process · Cathode · Mixed ionic-electronic conductor (MIEC) · Electrochemical impedance spectroscopy (EIS) · Area-specific-resistance (ASR)

Introduction

The electrical power generation systems based on solid oxide fuel cells (SOFCs) have attracted more attention compared to other energy conversion engines due to their high efficiency, fuel flexibility, and possibility to recover exhaust heat [1–9]. The major drawbacks with conventional SOFCs such as cell cracking, formation of non-conducting compound(s) at electrode–electrolyte interfaces, the need for expensive non-metallic interconnects, etc. have been due to very high operating temperature. One of the possible ways to overcome these problems has been to reduce the working/operating temperature within the range 500–800 °C; i. e., to focus attention on the development of intermediate-temperature solid oxide fuel cell (IT-SOFC). Nevertheless, achieving high cell performance at reduced temperature has posed great challenges before the scientists, engineers, and technologists involved in the development of IT-SOFC. IT-SOFC efficiency, crucially depends on cathode performance. The requirements of cathode have been, high-catalytic activity for oxygen reduction, comparable thermal expansion coefficient (TEC), high electrical conductivity, and compatibility with the other cell components.

In recent past, lanthanum strontium manganite (LSM) has been projected as a potential cathode material due to compatibility of its TEC with gadolinia-doped-ceria (GDC) and yttria-stabilized zirconia (YSZ) electrolytes. However, during fabrication or operation, it reacts with YSZ to form resistive pyrochlore La$_2$Zr$_2$O$_7$ and/or SrZrO$_3$ at the cathode–electrolyte interface [10]. In addition to this, it exhibits low oxygen-ion conductivity (10^{-7} S cm^{-1} at 900 °C). Both these factors prohibited its usage in IT-SOFC. The Sm$_{0.5}$Sr$_{0.5}$CoO$_3$, a good electronic conductor, has also been proposed as a promising cathode for IT-SOFCs [11, 12]. In near recent past, two typical perovskites the La$_{1-x}$Sr$_x$Co$_{1-y}$Fe$_y$O$_{3-\delta}$ and the Ba$_{1-x}$Sr$_x$Co$_{1-y}$Fe$_y$O$_{3-\delta}$, belonging to the class of mixed ionic-electronic conductors (MIECs), have been projected as alternative cathodes to LSM [13–17].

A literature survey revealed that the materials with K_2NiF$_4$-type structure exhibit excellent catalytic activity for oxygen reduction. Also, they showed good thermal stability and TEC=10.5–14.2×10^{-6} K^{-1} comparable with those of the commonly used solid electrolytes such as

A. P. Khandale · S. S. Bhoga (✉)
Department of Physics, RTM Nagpur University,
Nagpur 440033, India
e-mail: msrl.physics1@gmail.com

YSZ, GDC, and samarium-doped ceria (SDC) [18–21]. The K_2NiF_4 structure consists of perovskite (ABO_3) layers alternating with rock–salt (AO) layers; and it has been possible to incorporate excess of oxygen in the form of interstitial species into the rock–salt layers [22, 23]. Although the total conductivity and the TEC of $La_2Ni_{1-x}Cu_xO_{4\pm\delta}$ with K_2NiF_4-type structure have been fairly satisfactory, they exhibited rather high area-specific-resistance (ASR=1 ohm cm^2 at 850 °C) [24]. On the other hand, the ASR (0.24 ohm cm^2 at 700 °C) of $Nd_{1.7}Sr_{0.3}CuO_4$ cathode on SDC electrolyte has been found reasonable [25]. Similarly, $La_{2-x}Sr_xCuO_{4\pm\delta}$ gave low ASR (0.16 ohm cm^2 at 700 °C) [26].

The $Nd_{2-x}Ce_xCuO_{4\pm\delta}$ ($0 \leq x \leq 0.2$) solid solutions have been of special importance due to presence of extrinsic electrons as charge carriers. They exhibit T'-type tetragonal crystal structure consisting of copper–oxygen planes of CuO_2 wherein the copper ions have a square oxygen-ion neighborhood. Whereas, a sandwich formed by the layers of oxygen ions interspersed with neodymium/cerium ions [27]. Preliminary study on $Nd_{2-x}Ce_xCuO_{4\pm\delta}$ ($0 \leq x \leq 0.2$) with both the $Ce_{0.9}Gd_{0.1}O_{1.95}$ (GDC) and the $La_{0.9}Sr_{0.1}Ga_{0.8}Mg_{0.2}O_{3\pm\delta}$ (LSGM) electrolytes has shown high ASR [28]. A close scrutiny of the literature revealed that $Nd_{2-x}Ce_xCuO_{4\pm\delta}$ has not found much attention amongst cathode material for IT-SOFC viewpoint.

In the light of the above, the present study was aimed at the synthesis of $Nd_{2-x}Ce_xCuO_{4\pm\delta}$ ($0.1 \leq x \leq 0.25$) using sol–gel process. For a comparison, highest conductivity giving composition was also prepared by solid-state reaction. The prepared samples were characterized with the help of X-ray powder diffraction (XRD), scanning electron microscopy (SEM), and direct current (dc) conductivity. The electrochemical performance was evaluated using electrochemical impedance spectroscopy (EIS) and voltage versus current (V–I) characteristics, with a view to develop suitable solid cathode.

Experimental

The initial reagents Ce, Nd, and Cu in the form of nitrates with purity>99.9% were procured from Aldrich Chemicals (USA). Prior to the weighing, the above-mentioned reagents were dried at 120 °C for 6 h in order to remove the traces of moisture present. The requisite reagents, as per stoichiometry given in Table 1, were dissolved in the double-distilled deionised water separately. All these solutions were then mixed with pre-prepared 1.0 mol EDTA solution and citric acid by maintaining metal ions/EDTA/citric acid in 1:1:1.5 molar ratio. The pH of the mixture was maintained to 6.0 so as to obtain the homogeneous solution. Later, the homogeneous solution was heated while stirring until the formation of blue-colored gel. The gel was ignited at 250 °C to yield brown-colored powder. The powder, thus obtained, was calcined at 850 °C for 2 h. The pellets of 9 mm diameter and 1–2 mm thickness were obtained by uniaxially compressing calcined powder at 3 tons/cm^2 pressure with the help of Specac (UK) stainless steel die and hydraulic press. The pellets were finally sintered at 1,000 °C for 8 h. Alternatively, $Nd_{1.8}Ce_{0.2}CuO_{4\pm\delta}$, was also prepared using solid-state reaction method. Particularly, the dried oxide reagents in stoichiometric ratio were ball milled under acetone medium at 300 revolutions per minute (rpm) for 2 h. The well-ground mixture was then pelletised to obtained circular discs of 9 mm diameter as described above. Later the pellets were sintered at 1,000 °C for 24 h.

For electrochemical investigations, the slurry/ink of the $Nd_{1.8}Ce_{0.2}CuO_{4\pm\delta}$ cathode was obtained as follows. A gram of $Nd_{1.8}Ce_{0.2}CuO_{4\pm\delta}$ powder was mixed with 3 wt.% polyvinyl buteral (binder), sodium-free corn oil, and ethyl methyl ketone. The mixture was then ball milled using a planetary monomill (Fritsch Pulverisette-6, Germany) for 2 h with 300 rpm. The GDC (10 mol.% gadolinium-doped ceria) nanopowder (Aldrich, USA) was pressed in a similar manner to obtain pellets of 9 mm diameter and 1–2 mm thickness. They were then sintered at 1,400 °C for 6 h. A sintered density of about 96% was achieved. Both flat surfaces of the GDC pellet were then roughened with #60 grid paper and cleaned with acetone. The slurry/ink of each cathode material was then spin-coated at 3,000 rpm for 60 s on both flat surfaces of the sintered GDC electrolyte to obtain the symmetric cells of configuration, $Nd_{1.8}Ce_{0.2}CuO_{4\pm\delta}$/GDC/$Nd_{1.8}Ce_{0.2}CuO_{4\pm\delta}$.

The symmetric cells were first baked at 600 °C for 2 h to burn out the organic binders and finally sintered at various temperatures. The details of cell preparative parameters are given in Table 3.

Table 1 Compositions, lattice cell constants (a, c, and v), crystallite size (C_s), crystal lattice strain (S_l), and sinter density (ρ) of $Nd_{2-x}Ce_xCuO_{4\pm\delta}$ (x=0.1, 0.15, and 0.2) prepared by sol–gel and $Nd_{1.8}Ce_{0.2}CuO_{4\pm\delta}$ prepared by solid-state reaction

Composition	Code	a (nm)	c (nm)	v (nm^3)	C_s (nm)	S_l (%)	ρ (%)
$Nd_{1.9}Ce_{0.1}CuO_{4\pm\delta}$	NCCO-0.1(SG)	0.395	1.213	0.190	233.9	0.12	84.11
$Nd_{1.85}Ce_{0.15}CuO_{4\pm\delta}$	NCCO-0.15(SG)	0.394	1.210	0.189	169.2	0.23	85.61
$Nd_{1.8}Ce_{0.2}CuO_{4\pm\delta}$	NCCO-0.2(SG)	0.395	1.208	0.188	157.2	0.26	86.77
$Nd_{1.8}Ce_{0.2}CuO_{4\pm\delta}$	NCCO-0.2 (SSR)	0.395	1.209	0.189	215.2	0.129	85.10

All the sintered samples were characterized by X-ray powder diffraction (XRD) using PANalytical X'pert PRO (Philips, Holland), which employed Cu K_α radiations. The curved graphite crystal was used as a monochromator. The X-ray diffraction measurements were carried out in the 2θ range from 10° to 80° with the step size and time per step as 0.020° and 5 s, respectively. The microstructures of fractured pellets were examined with the help of SEM, JEOL JSM-6380A. The density of the sintered pellets was measured following Archimedes principle with the help of Mettler XS105 dual range monopan balance with density kit attachment and built in density measurement software. The theoretical (X-ray) density of each composition was taken from respective JCPDS data to evaluate sintered density.

The thin platinum film on both the flat surfaces of the sintered pellet was obtained by dc sputtering, and resulted in good ohmic contacts for dc electrical conductivity measurements. Prior to the conductivity measurement, the sample was spring-loaded in a ceramic cell holder (Amel, Italy) and heated to 700 °C for 1 h so as to homogenize the charge carriers. The resistance as a function of temperature, during the cooling cycle, was measured following four-probe method with the help of computer-controlled Keithley 6221 current source and Keithley 2182A nanovoltmeter in delta mode. The temperature of the sample was controlled with an accuracy of ±1 °C using Eurotherm 2216e temperature controller. The tip of a calibrated thermocouple was kept in the vicinity of the sample to measure the actual sample temperature.

Electrochemical impedance measurements on the sintered symmetric cells were carried out using a computer-controlled Solartron 1255B FRA in combination with a Solartron SI 1287 electrochemical interface. Prior to the impedance measurement, the spring-loaded samples were heated to 700 °C. During the cooling cycle, a dwell time of 30 min. was given at each set temperature to ensure thermal equilibrium in the cells. Ten minutes prior to the end of the dwell time, the real, and the imaginary parts of the impedance were measured as a parametric function of frequency and temperature in the range of 0.01 to 1×10^6 Hz and 480 to 700 °C, respectively, with a signal amplitude of 50 mV. The desired concentration of O_2 gas (Po_2) was engineered by mixing high purity grade oxygen with nitrogen using electronic mass flow controllers (Teledyne-Hastings, USA). The EIS data obtained were analyzed using Scribner advanced software for electrochemical research and development [29]. The voltage–current characteristic of symmetric cell was obtained at different temperatures. During measurements the voltage was scanned from +0.7 to −0.7 V with the step of 5 mV/s using Solartron SI1287 electrochemical interface.

Results and discussion

X-ray powder diffraction

Typical X-ray powder diffraction patterns of $Nd_{2-x}Ce_xCuO_{4\pm\delta}$ with x=0.1–0.25 are shown in the Fig. 1a–d, respectively. A close look at the Fig. 1a reveals that the entire characteristic diffracted lines matched closely with the JCPDS (joint committee for powder diffraction standard) data (File No. 01-084-2177) corresponding to tetragonal Nd_2CuO_4. Similarly, all the diffracted lines appeared in Fig. 1b and c, match closely with the JCPDS data due to tetragonal Nd_2CuO_4, except small deviations. No line, either due to initial reagents or any intermediate phase is seen in the cases of x=0.1, 0.15, and 0.2. On the other hand, in case of x=0.25 (Fig. 1d) in addition to the lines due to Nd_2CuO_4, few weak diffracted lines due to CeO_2 are present. The absence of line(s) corresponding to pure reagents as well as of any intermediate phases for $x\leq0.2$ confirms the formation of single-phase tetragonal $Nd_{2-x}Ce_xCuO_{4\pm\delta}$ solid solution up to x=0.2. In case of x>0.25, the cerium precipitates in the $Nd_{1.8}Ce_{0.2}CuO_{4\pm\delta}$ solid solution matrix. The formation of $Nd_{1.8}Ce_{0.2}CuO_{4\pm\delta}$ solid solution prepared by solid-state reaction was confirmed in a similar way. Spinolo et al. have also reported the solid solubility limit up to x=0.2 [27]. In order to ascertain the formation of solid solution and its consequence on host structure, the lattice cell constants for all the samples under study were determined using Unitcell, computer software developed by Holland and Redfern [30]. The values of lattice cell constants a, c, and v of all solid solutions are compared in Table 1. Evidently, the lattice cell constant along a-axis does not change with the dopant concentration. On the other hand, cell constant c decreases with an increase in Ce content in $Nd_{2-x}Ce_xCuO_{4\pm\delta}$ up to x=0.2. These results substantiate the solid solubility limit of Ce in Nd_2CuO_4 up to x=0.2. The Nd_2CuO_4 lattice contraction along the c-axis from
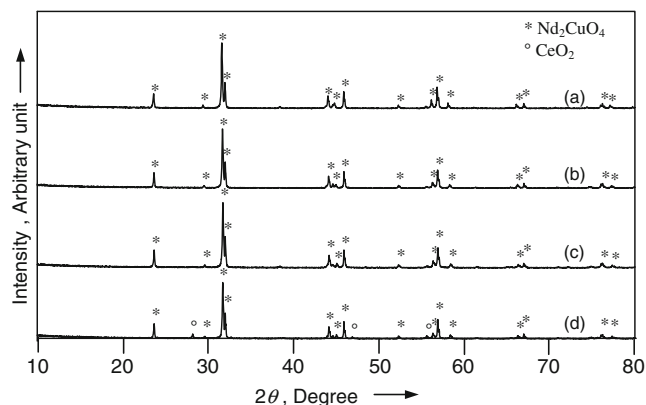

Fig. 1 The X-ray powder diffraction patterns of $Nd_{2-x}Ce_xCuO_{4\pm\delta}$ with **a** x=0.1, **b** x=0.15, **c** x=0.2, and **d** x=0.25

12.15 to 12.07Å when doped with 7.5 mol.% Ce has also been observed earlier [31]. According to Kim and Kvam, Ce remains tetravalent and occupies eight-coordinated Nd^{3+} site in T' type Nd_2CuO_4 structure. The ionic radius of eight-coordinated Ce^{4+} is 0.097 nm [32], which is smaller than that of eight-coordinated host Nd^{3+}, $r_i =$ 0.101 nm [31]. Consequently, the host lattice contracts due to the partial substitution of the latter for the former. In the T' type Nd_2CuO_4 crystal structure the coordination of Cu ions is 4 due to absence of apical oxygen, and single CuO_2 plane exists in the unit cell. The coupling between the CuO_2 layers along the c-axis is expected to be weaker leading to an anisotropic lattice cell contraction. Voronin et al. have given a detailed justification for the lattice contraction along the c-axis due to partial replacement of Nd^{3+} by Ce^{4+} in Nd_2CuO_4 [31]. They have also reported a negligible change in the value of a with x.

The crystallite size of all solid solutions was obtained using X'pert Highscore plus software based on Debye Scherrer formulae,

$$C_s = \frac{0.9\lambda}{\beta \cos\theta_B} \tag{1}$$

where C_s, λ, and θ_B are crystallite size, X-ray wavelength, and Bragg angle, respectively. Here, β was obtained using relation given below,

$$\beta^2 = \beta_m^2 - \beta_s^2 \tag{2}$$

where, β_m and β_s were the measured and the standard full width of half maxima of diffracted line, respectively. The β_s

was estimated from the XRD pattern obtained by running the experiment on standard silicon sample provided by PANalytical, Netherlands. The experimental crystallite size of $Nd_{2-x}Ce_xCuO_{4\pm\delta}$ with x=0.1–0.2 is compared in Table 1. The grain size of all the $Nd_{2-x}Ce_xCuO_{4\pm\delta}$ solid solutions, in general, is (Table 1) in the range of 150–230 nm. The crystallite size reduces with increased x. Aguadero et al. [24] and Chaker et al. [33] have also reported change in crystallite size due to metal cation doping. A comparison (Table 1) of crystallite size of $Nd_{1.8}Ce_{0.2}CuO_{4\pm\delta}$ prepared by sol–gel (NCCO-0.2(SG)) and by solid-state reaction (NCCO-0.2(SSR)) reveals smaller crystallite size of former than that of latter. Furthermore, an increased lattice strain (Table 1) with x, compliments the reduced grain size after doping. A close look at the Table 1 reveals that the sintered density of $Nd_{2-x}Ce_xCuO_{4\pm\delta}$ increases with increase in Ce content. Furthermore, the sintered density of NCCO-0.2(SSR) is lesser than that of NCCO-0.2(SG). Increased sintered density with enhanced Ce content in $Nd_{2-x}Ce_xCuO_{4\pm\delta}$ is attributed to the reduction in the grain size.

Scanning electron microscopy

The SEM of the cleaved NCCO-0.1(SG), NCCO-0.15(SG), NCCO-0.2(SG), and NCCO-0.2(SSR) are displayed in Fig. 2a, b, c, and d, respectively. In general, 90% of the cleaved surface consists of trans-granular cleavages and the other consists of voids/pores and grain boundaries for all samples. Particularly, the grain size reduces from submi-
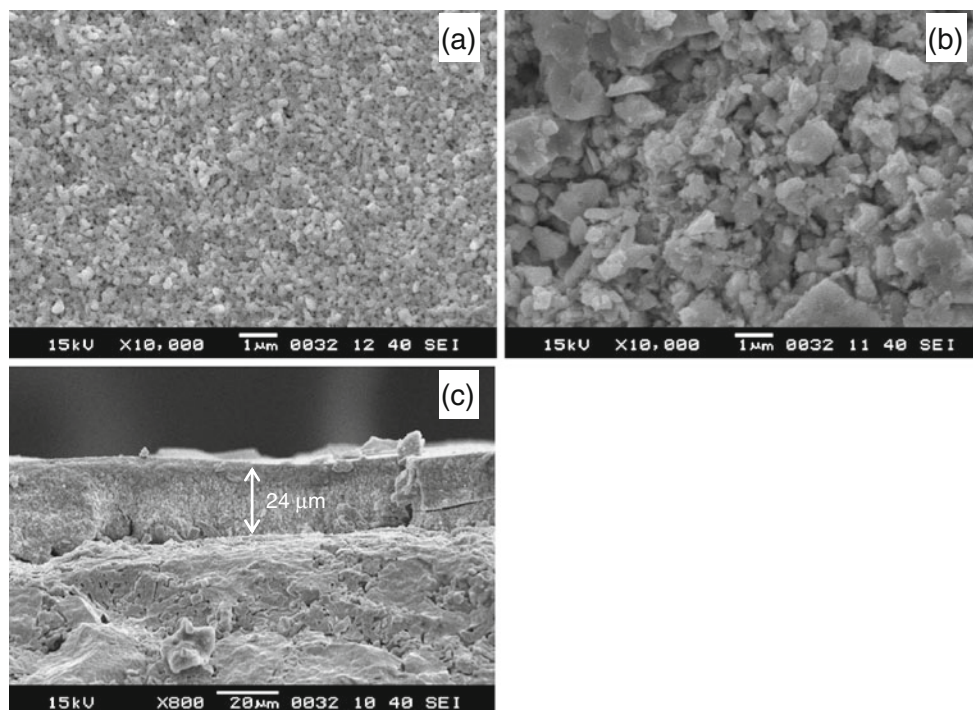

Fig. 2 Scanning electron microphotographs of **a** NCCO-0.1 (SG), **b** NCCO-0.15(SG), **c** NCCO-0.2(SG), and **d** NCCO-0.2 (SSR)
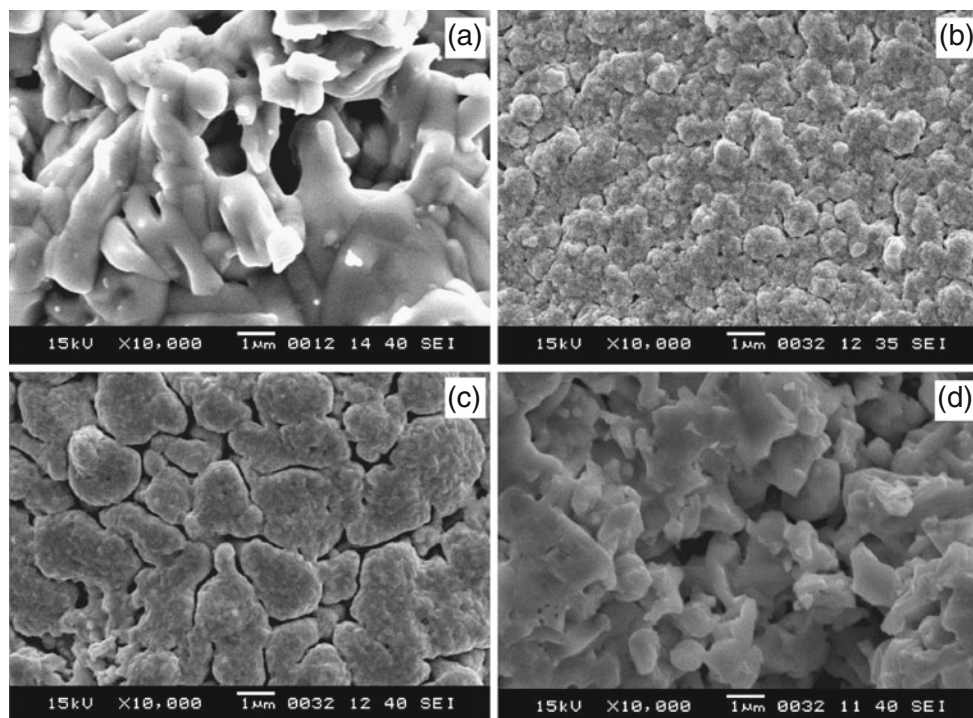
cron to nano size with an increased x in $Nd_{2-x}Ce_xCuO_{4\pm\delta}$. Furthermore, the nano-sized grains agglomerate to form lumps of about a micrometer, which introduces (Fig. 2b and c) nano/submicron pores. Moreover, arrangement of these lumps further gives micron size pores in the sample. A comparison of Fig. 2c and d reveals smaller grain size of NCCO-0.2(SG) than that of NCCO-0.2(SSR). Also, the grains of former are spherical and uniform, whereas, grain size and grain shape of latter are non-uniform and irregular. The difference in sintered densities (Table 1) of NCCO-0.2(SG) and NCCO-0.2(SSR) is attributed to the disparity in size and shape of grains resulted from dissimilarity in preparative techniques.

The SEM photographs of cathode surface for cell-8, cell-12 and fractured surface across the electrode–electrolyte interface of cell-8 are depicted in Figs. 3a-c, respectively. As seen, the grains of cathode sintered at 800 °C are of nano size (Fig. 3a), which grow further to micron size due to sintering at 1,200 °C (Fig. 3b). Furthermore, such nanocrystalline $Nd_{1.8}Ce_{0.2}CuO_{4\pm\delta}$ grains are uniformly distributed throughout the cathode, which results in evenly distributed nanopores throughout the cathode layer. The sintering of symmetric cell at 1,200 °C facilitated fusion of nanocrystalline $Nd_{1.8}Ce_{0.2}CuO_{4\pm\delta}$ grains that led to grain growth (Fig. 3b). A close look at the Fig. 3c reveals that the electrode and the electrolyte form intimate contact all along the interface. Moreover, electrode–electrolyte interface is homogeneous. The electrode layer thickness is ≈24.0 μm. Furthermore, the grains of GDC electrolyte are bigger than those of $Nd_{1.8}Ce_{0.2}CuO_{4\pm\delta}$ cathode.
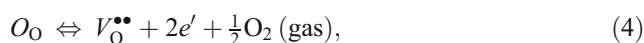
DC four-probe conductivity

The variation of dc conductivity with temperature for all the samples under study is shown in Fig. 4. All the samples exhibit negative temperature coefficient (NTC) to positive temperature coefficient (PTC) transition at about 620 °C. Below transition temperature all the samples obey the Arrhenius law,

$$\sigma T = (\sigma T)_0 \exp\left(\frac{-E_a}{kT}\right), \qquad (3)$$

where σ, $(\sigma T)_0$, k, T, and E_a are dc conductivity, pre-exponential factor, Boltzmann constant, absolute temperature, and activation energy, respectively. A close scrutiny of Fig. 4 suggests that σ enhances continuously with an increase in Ce concentration in $Nd_{2-x}Ce_xCuO_{4\pm\delta}$. The activation energies for all the samples, however, remain unchanged with Ce dopant concentration. Furthermore, the conductivity of NCCO-0.2(SG) is higher than that of NCCO-0.2 (SSR). The higher dc conductivity in the former solid solution compared to the latter one is due to its effective smaller grain size, uniform spherical grain shape, and higher sinter density.

As a matter of fact, intrinsically the electrons and the holes can be produced in $Nd_2CuO_{4\pm\delta}$ lattice by two point defect equilibria given below using Kröger–Vink notations [34]:

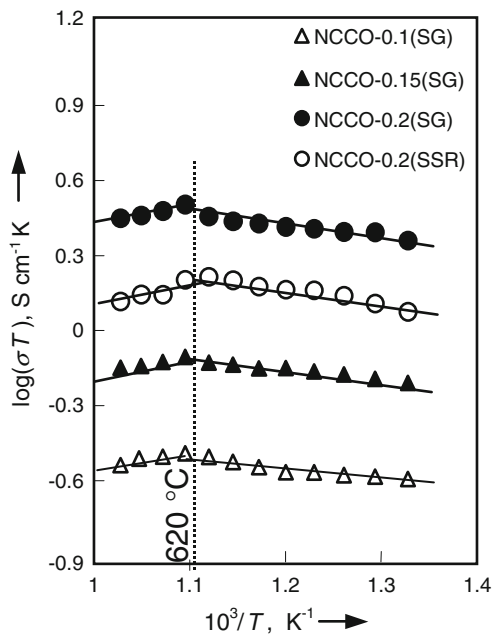$$O_O \Leftrightarrow V_O^{\bullet\bullet} + 2e' + \tfrac{1}{2}O_2 \text{ (gas)}, \qquad (4)$$

Fig. 3 Scanning electron micro-photographs of electrode surface of **a** cell-8 and **b** cell-12, and **c** electrode–electrolyte interface of cell-8

Fig. 4 Arrhenius plots for NCCO-0.1(SG), NCCO-0.15(SG), NCCO-0.2(SG), and NCCO-0.2(SSR)

$$\tfrac{1}{2}O_2(gas) \Leftrightarrow O''_i + 2h^\bullet, \tag{5}$$

coupled with intrinsic ionization:

$$nil \Leftrightarrow e' + h^\bullet \tag{6}$$

where, O_O, $V_O^{\bullet\bullet}$, O''_i, e' and $h^\bullet$ are oxygen at its regular lattice site, oxygen vacancy with two positive charges in the lattice, oxygen interstitial with two negative charges, electron with its negative charge and hole with its positive charge, respectively. Furthermore, it has been proposed that extra electrons can be introduced both by equilibrium between intrinsic point defects and external O_2 (Eq. 4 or Eq. 5 coupled with Eq. 6, or both) [27]. According to literature, both oxygen interstitials (O''_i) and oxygen vacancies ($V_O^{\bullet\bullet}$) are present in $Nd_2CuO_{4\pm\delta}$ [27, 35]. The e' and $h^\bullet$ defects are more or less bound to Cu regular sites. Since the dc conductivity measurements are taken at 1 atm pressure of oxygen, the temperature dependent dc conductivity behavior is consistent with equilibria (5) and (6) involving thermally activated point and electronic defects. In addition to this, partial substitution of Ce^{4+} for Nd^{3+} introduces extrinsic defects according to quasichemical reaction given below using Kroger–Vink notations,

$$CuO + 2CeO_2 \rightarrow Cu_{Cu}^x + 2Ce_{Nd}^\bullet + 4O_o^x + 2e' + \tfrac{1}{2}(O_2). \tag{7}$$
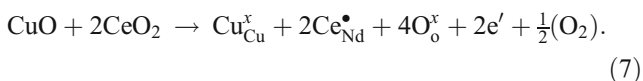
where Cu_{Cu}^x and $Ce_{Nd}^\bullet$ denote Cu at regular Cu lattice site and Ce with additional positive charge at Nd lattice site, respectively. The electrons, thus created, are associated with the CuO_2 planes. The concentration of extrinsically created

electrons in CuO_2 planes due to Ce doping increases with increased Ce concentration [27]. The increase in electron concentration has been supported by Hall coefficient measurements [27, 36]. In the present case, the doping with aliovalent Ce affects the nature and the amount of electronic carriers more strongly than the intrinsic point defects (Eqs. 5 and 6). This is because with heavy doping the intrinsic defects are buffered by the extrinsic defects. Thus, the dc conductivity of $Nd_{2-x}Ce_xCuO_{4\pm\delta}$ increases considerably with increase in Ce content in it (Fig. 4).

Electrochemical impedance spectroscopy

Typical electrochemical impedance spectra (EIS) of cell-8 at various temperatures are depicted in Fig. 5a. The impedance spectra shown in Fig. 5a revealed a distorted semicircular arc in the low-frequency region. The incomplete semicircular arc in the high-frequency region is attributed to the limitation of the Solartron 1255B FRA for high frequencies (≤1 MHz). The low-frequency semi-

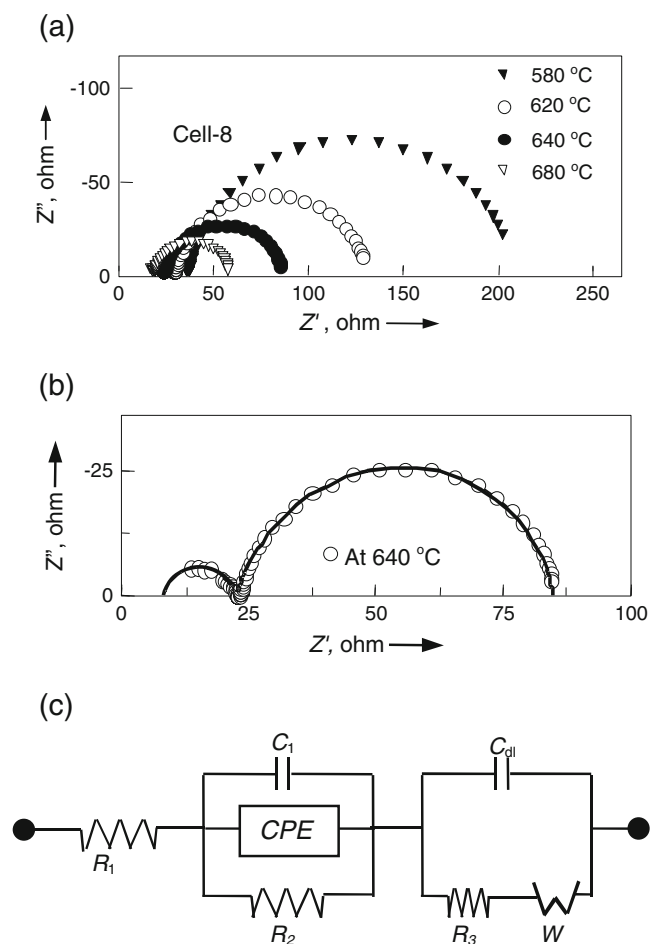(a)

(b)

(c)

Fig. 5 Electrochemical impedance plots **a** at various temperatures for cell-8, **b** experimental EIS data measured at 640 °C and simulated EIS response, and **c** electrical equivalent circuit model

circular arc is due to complex electrode process, such as the passage of current through the electrode as well as across the electrode–electrolyte interface and absorption as well as reduction of O_2 at cathode. The incomplete high-frequency semicircular arc is attributed to the passage of current through GDC electrolyte. Low-frequency semicircular arc (due to electrode) indicates the reversible reduction of O_2 gas at cathode, and subsequently migration of the O^{2-} across the electrode-electrolyte interface. In general, increase in real axis intercepts of low as well as high-frequency semicircular arcs with decrease in temperature is evident from Fig. 5a. Such behavior implies increased ASR (electrode polarization) and electrolytic resistance with reduction in temperature. Almost similar behavior of impedance spectra was observed for cell-8(SSR) and cell-12.

A typical EIS data along with the simulated response and electrical equivalent circuit model are shown in Fig. 5b and c, respectively. Evidently, the EIS response (solid line) simulated using electrical equivalent model (Fig. 5c) fitted well with the experimental data (open circles in Fig. 5b). The resistance R_2 in parallel with geometrical capacitance of electrolyte (C_1) represents the ion migration through the GDC electrolyte. The constant phase element (CPE) in parallel with R_2 as well as C_1 takes care of depression in high-frequency semicircular arc. The R_1 in equivalent circuit represents the lead resistance. Finite length Warburg impedance (W) in series with the R_3 is attributed to the reactions of diffusing species and subsequent migration. The C_{dl} is the double layer capacitance. Similar EIS data simulation using equivalent circuit has been demonstrated elsewhere [37]. The values of simulated electrical circuit elements at various temperatures are displayed in Table 2. As seen, the leads resistance R_1 does not vary appreciably with change in temperature. On the other hand, the resistances R_2 and R_3 corresponding to electrolytic and electrode, respectively increase with reduction in temperature, which is in good agreement with the EIS plots (Fig. 5a). Furthermore, the values/magnitudes of parameters CPE-T and W-T corresponding to CPE and Warberg impedance, respectively, increase with reduction in temperature.

The low-frequency semicircular arcs (Fig. 5a and b) exhibit response similar to that of finite length Warburg

impedance observed for reversible electrodes [38]. Warburg impedance (Z_w) is represented by the following expression,

$$Z_w = \sigma_w \Big/ \left(\omega^{1/2} \right) - j\sigma_w \Big/ \left(\omega^{1/2} \right), \text{ here} \qquad (8)$$

$$\sigma_w = \frac{RT}{n^2 F^2 A \sqrt{2}} \left[\frac{1}{D_O^{1/2} C_O^b} + \frac{1}{D_R^{1/2} C_R^b} \right],$$

and ω is the angular frequency. The subscripts O and R represent the oxidized and reduced states of the species, and C^b denotes a bulk concentration. D is the diffusion coefficient of the species. The value of the Warburg impedance depends on the frequency of the perturbation. At relatively higher frequencies, the Warburg impedance is smaller since the reactants do not move far. Conversely, at lower frequencies, since the reactants have a greater length to travel, the Warburg impedance is higher. As a consequence the EIS curve corresponding to electrode is nearly straight line at relatively higher frequencies followed by a semicircle as seen in Fig. 5b. Thus, low-frequency semicircular arc is attributed to $Nd_{1.8}Ce_{0.2}CuO_{4\pm\delta}$ electrode.

Materials involving conduction via ion-hopping, the immediate microscopic surroundings of different ions would be distinct at a given instant due to either micro-heterogeneity in it [39] or the dynamic relaxation of the positions of atoms surrounding an ion progresses in different amount for unlike ions [40, 41]. In both the cases, they are described in terms of the distributed relaxation times, arising due to dispersal in activation enthalpies for ion migration. Because the small differences in activation energies (E_a) can lead to large differences in relaxation times τ according to

$$\tau = \tau_0 \exp\left(\frac{E_a}{kT} \right) \qquad (9)$$

The physical models have stressed distribution in τ [42]. Macdonald and Brachman have provided a useful set of integral transform relations between distribution functions and electrical response [43]. Van Weppner et al. have developed a theory, based on dipole–dipole interactions, that leads to almost Gaussian distribution of activation energies [44].

Table 2 The values of fitted electrical circuit elements corresponding to EIS data of cell-8 at various temperatures

Sr. number	T (°C)	R_1 (ohm)	R_2 (ohm)	CPE-T	CPE-P	C_{dl} (F)	R_3 (ohm)	W-R (ohm)	W-T	W-P
1	680	8.72	9.7	0.9×10^{-7}	0.79	7.2×10^{-6}	7.0	32	0.0010	0.41
2	640	8.71	14.4	2.0×10^{-7}	0.76	1.2×10^{-6}	9.3	55	0.0015	0.41
3	620	8.72	19.0	5.3×10^{-7}	0.76	9.2×10^{-7}	11.0	89	0.0029	0.41
4	600	8.70	22.9	9.3×10^{-7}	0.75	5.2×10^{-7}	12.3	188	0.0050	0.41
5	580	8.71	37.0	0.9×10^{-6}	0.76	1.3×10^{-7}	12.9	291	0.0090	0.41

Ravain and Souquet [45], for the first time, have introduced CPE element in electrical equivalent model for glassy solid electrolyte (similar to shown in Fig. 5b) to account the depressed semicircle in complex impedance plane thereby distribution in τ, of the form

$$Z_{CPE} = A(j\omega)^{-\alpha} \tag{10}$$

here α, a measure of depression of semicircular arc in complex impedance plane, lies between 0 and 1. Later Raistric et al. have applied it to polycrystalline solid electrolyte [46]. Subsequently, CPE element has been frequently used in parallel with geometrical capacitance, C, and electrolytic bulk resistance, R [47, 48]. Detailed theoretical description and electrical equivalent circuit for distributed relaxation time (depression in complex impedance plots) have been given in literature [49].

In case of reversible electrode, the current is limited by either slow charge transfer kinetics, or by a process such as adsorption, which effectively controls the concentration of reactants or products. This leads to a concentration gradient leading to the formation of space charge (double layer) capacitance. This has been viewed as a familiar situation to a single step charge transfer reaction [50].The rate of single step charge transfer reaction

$$O + ne = R \tag{11}$$

is given by the expression

$$i_F = nF[k_f c_O - k_b c_R] \tag{12}$$

where i_F, k_f, and k_b are faradic current density, forward, and reverse rate constants, respectively. c_O and c_R are the concentrations of the reactants and products at the interface, respectively at time t. Such concentration difference in reactants O and product R leads to space charge (double layer) capacitance. The current, in general, is composed of a steady state or dc part determined by the mean dc potential E and the mean dc concentrations at the interface, c_O and c_R. The ac part, Δi_F, is determined by the ac perturbing potential ΔE and the fluctuating concentrations Δc_i. The complete equivalent circuit for a single-step charge transfer reaction in the presence of diffusion has been Randles circuit as shown in Fig. 5c (low-frequency response) [49]. Similar circuit has been used to investigate the interfacial kinetics, and solid-state diffusion of lithium insertion reaction into perovskite tungsten bronzes [51], and Li-WO$_3$ [52]. Thomas et al. have also proposed presence of C_{dl} in equivalent circuit for insertion LiCoO$_x$ electrode to account for ion concentration gradient at the electrode–electrolyte interface [53].

The electrolytic bulk conductivity, σ_{GDC}, under air is obtained following relation,

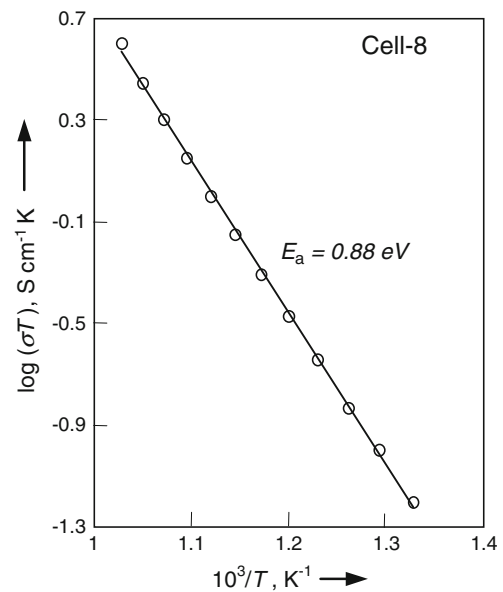$$\sigma_{GDC} = \frac{1}{R} \frac{t}{S}, \tag{13}$$

Fig. 6 Arrhenius plots for ionic conductivity of GDC electrolyte obtained from cell-8

here R, t, and S are the electrolytic resistance, thickness, and the surface area of GDC electrolyte, respectively. The electrolytic resistances, R, for cell-8 were obtained at various temperatures from x-axis intercept of high-frequency semicircles (Fig. 5). The Arrhenius plot for GDC is shown in Fig. 6. The activation energy E_a=0.88 eV, determined from Arrhenius plot (log σT Vs $10^3/T$), is in close agreement with the earlier reported value, E_a=0.9 eV [54]. Thus, the high-frequency semicircle appeared in complex impedance plane attributed to migration of O^{2-} through GDC electrolyte is justified.
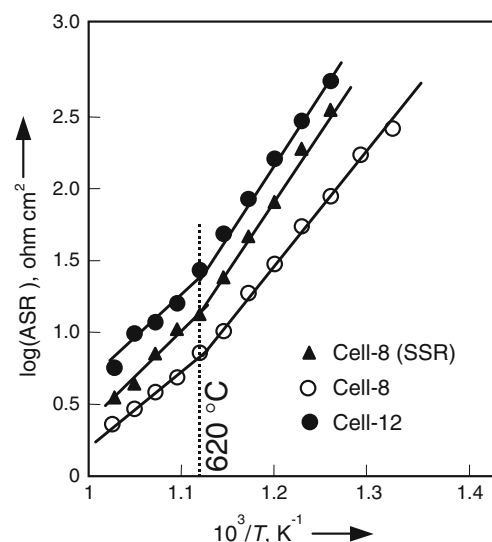

Fig. 7 Arrhenius plots of area-specific resistance (ASR) for cell-8 (SSR), cell-8, and cell-12

Table 3 A comparison of ASR and activation energies for cell-8(SSR), cell-8, and cell-12

Sr. number	Cathode	T_s (°C)	Cell-code	ASR at 700 °C (ohm cm^2)	E_a (eV)	E_a* (eV)
1	NCCO-0.2(SSR)	800	Cell-8 (SSR)	2.03	1.63[a]	1.68[a]
					1.94[b]	1.88[b]
2	NCCO-0.2(SG)	800	Cell-8	0.93	1.52[a]	1.67[a]
					1.79[b]	1.87[b]
3	NCCO-0.2(SG)	1200	Cell-12	3.92	1.83[a]	1.90[a]
					2.35[b]	2.26[b]

T_s sintering temperature, E_a activation energy determined from ASR plots, E_a* activation energy determined from peak frequency plots

[a] High-temperature region

[b] Low-temperature region

A comparison of temperature dependent ASR of the symmetric cell-8(SSR), cell-8, and cell-12 is given in Fig. 7. The transition at 620 °C is clearly seen in all cells. The observed values of T_c are in good agreement with the NTC to PTC transition temperatures (Fig. 4). The ASR below and above the transition temperature obeys the Arrhenius law. The activation energies in the low and the high temperature regions for cell-8(SSR), cell-8, and cell-12 are compared in Table 3. A close scrutiny of the Table 3 as well as Fig. 4 reveal that the ASR corresponding to the cell-8 is lowest amongst all cells under study. Lowest ASR for cell-8 is attributed to the smallest grain size compared to other cell. The sintering of symmetric cell at 1,200 °C (cell-12) gives rise to the grain growth (Fig. 3b), which in turn reduces the effective electrochemically active $O_2/Nd_{1.8}Ce_{0.2}CuO_{4\pm\delta}$ phase boundary thereby inferior electrochemical properties of cell-12 than cell-8.

The Arrhenius like behavior of relaxation time seen in Fig. 8 is associated with the electrode reaction/mechanism. Here, also, the observed transition at about 620 °C coincides with the transition in temperature dependent ASR (Fig. 7). A hopping theory proposed by Salamon [55] is extended to the polarons in present case. During the mobility of polaron, along with the charge lattice distortion also moves. This process is often referred to as hopping mechanism. According to Salamon, the migration of charge carriers in solids can be visualized as their hopping from occupied positions in the lattice to nearby equivalent vacant positions by traversing a barrier of height E_a at the rate of,

$$f_p = f_0 \exp\left(\frac{E_a^*}{kT}\right), \tag{14}$$

here, f_p, f_0, and E_a^* are jump/hopping frequency, hopping attempt frequency, and activation energy, respectively. The peak frequency of electrochemical impedance,

$$\omega_{max} = 2\pi f_p = \frac{1}{\tau} = \frac{1}{RC} = \frac{\sigma}{\varepsilon\alpha\mu C}, \tag{14a}$$

$$\mu = \mu_0 \exp\left(\frac{-E_m}{kT}\right) \tag{14b}$$

where, μ and E_m denote the mobility and the migration enthalpy, respectively. μ_0 is proportional to jump attempt frequency of mobile charge carriers. Substitution of Eq. 14b in 14a and reorganization leads to Eq. 14. In addition to the polarons, oxygen ions also migrate via hopping mechanism in electrode. The activation energies determined using Eq. 14 are compared in Table 3. Evidently, the activation energies for cell-8(SSR), cell-8, and cell-12 in low- and high-temperature regions match closely with those of activation energies determined from temperature dependent ASR plots (Fig. 7). These results indicate that the charge transfer within the electrode as well as across the electrode–electrolyte interface is via hoping mechanism. Similar results have been reported earlier [56].
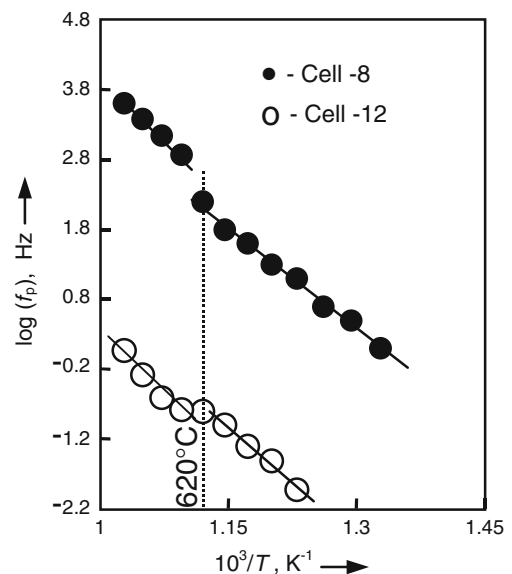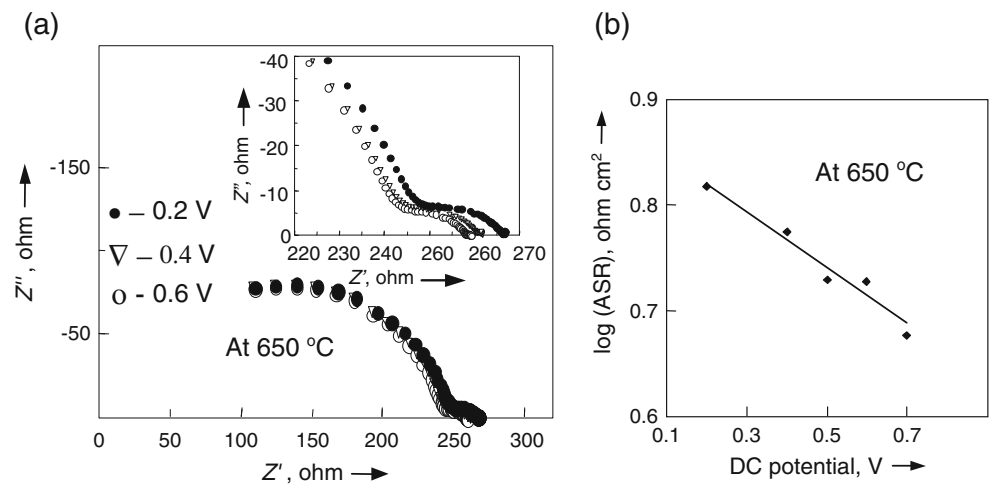

Fig. 8 Arrhenius plots of electrode relaxation frequency, f_p, obtained for cell-8, and cell-12

Fig. 9 (a) Electrochemical impedance plots of cell-8 at 650 °C under different dc polarization voltage; insert shows exploded view and (b) variation of ASR with dc polarization voltage
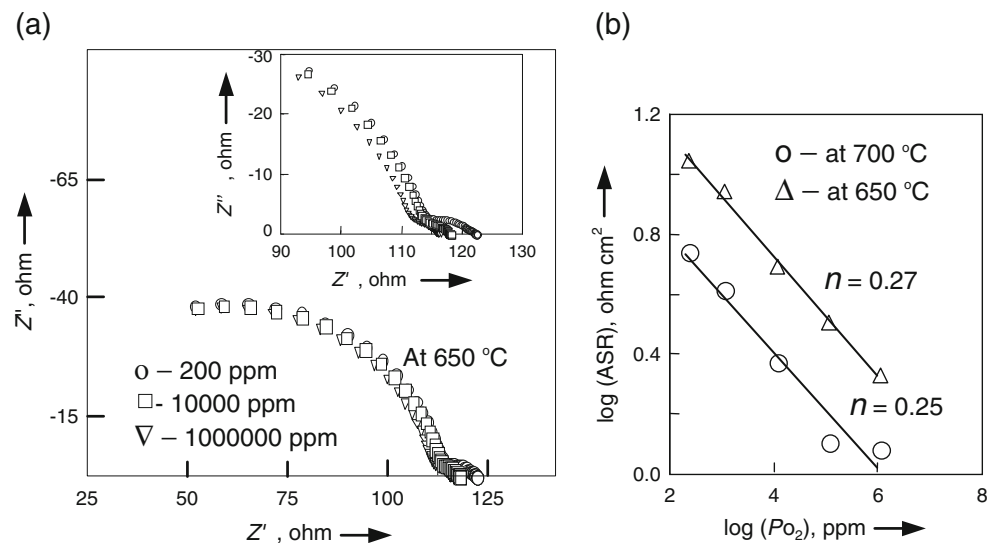

The electrochemical impedance plots for cell-8 under different dc biasing voltage at 650 °C and dc-biased voltage-dependent ASR are depicted in Fig. 9a and b, respectively. From the inset of Fig. 9a and b it is seen that, in general, the ASR reduces with an increased biasing voltage. The increase in ASR with increased dc potential (Fig. 9b) is in agreement with the earlier reporting [56, 57].

The electrochemical impedance plots at 650 °C for different values of P_{O_2} around cell-8 are depicted in Fig. 10a. In general, the x-axis intercept of low-frequency semicircular arc increases, inset of Fig. 10a, with decrease in P_{O_2}. Furthermore, the electrolytic bulk resistance/conductivity is least affected by the variation of P_{O_2}. The variation of log(ASR) at 650 and 700 °C with log(P_{O_2}) shown in Fig. 10b suggests a linear dependence of the former on the latter. This implies that the ASR varies with the oxygen partial pressure according to the relation given below,

$$\mathrm{ASR} = \mathrm{ASR}_0 (P_{O_2})^n \tag{15}$$

The value of n gives useful information about the type of species involved in the reactions at the electrode [58].

$$n = 1, \quad O_2(g) \Leftrightarrow O_{2,\mathrm{abs}} \tag{16}$$

$$n = \frac{1}{2}, \quad O_{2,\mathrm{abs}} \Leftrightarrow 2O_{\mathrm{abs}} \tag{17}$$

$$n = \frac{1}{4}, \quad O_{\mathrm{abs}} + 2e' + V_O^{\bullet\bullet} \Leftrightarrow O_O^x \tag{18}$$

The $n = 0.27$ and 0.25 at 650 and 700 °C, respectively (estimated from Fig. 10a in the present study) indicates absorption of oxygen in oxide lattice. The oxygen thus absorbed results into the electron and the vacancy for oxygen according to relation (18). The increased concentration of such created both the oxygen vacancies and the electrons in the oxide lattice with increased P_{O_2} are the key factors for reduced ASR, Fig. 10b.

Fig. 10 (a) Electrochemical impedance plots at different oxygen partial pressures; insert shows exploded view and (b) variation of log(ASR) with log(P_{O_2}) for cell-8
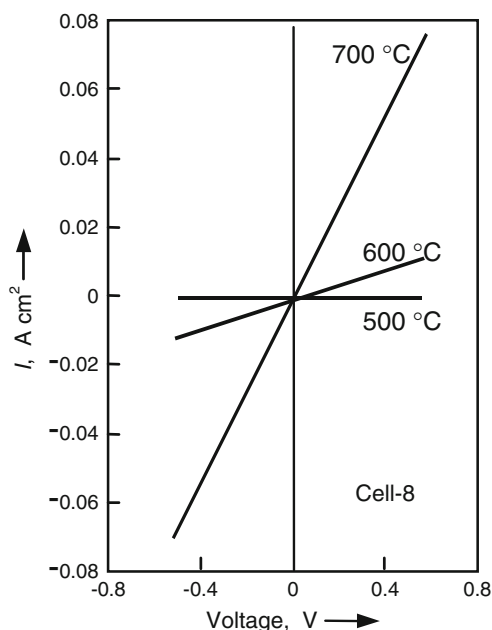
Fig. 11 Variation of current density with applied voltage across cell-8 at various temperatures

Current–voltage characteristics

The electrolytic ohmic contribution, determined from EIS studies on symmetric cell-8, was subtracted to obtain cathode overpotential. The variation of cathode overpotentials of the cell-8 at various temperatures is shown in Fig. 11. In general, an ohmic behavior is seen at all temperatures. The interfacial polarization resistances, also known as ASR, obtained at various temperatures from Fig. 11 are given in Table 4. A close scrutiny of Table 4 reveals an increase in cathode overpotential with decrease in temperature. Furthermore, ASRs obtained from current versus voltage data (Fig. 11) agree well with those obtained from EIS data (Table 4). The chemical and electrochemical reactions at $Nd_{1.8}Ce_{0.2}CuO_{4\pm\delta}$ cathode along with charge transfer across the cathode–electrolyte interface being thermally activated processes; the decrease in operating temperature of cell increases the overall cell resistance. Such increase in resistance with reduced temperature

eventually increases overpotential. Murray and Barnett have reported comparable ASRs determined from EIS and voltage–current characteristics for LSM-GDC composite electrode with YSZ as electrolyte [59]. A close scrutiny of Table 4 reveals that the $Nd_{1.8}Ce_{0.2}CuO_{4\pm\delta}$ cathode exhibited the lowest ASR compared to the MIEC cathodes reported earlier. The low ASR for $Nd_{1.8}Ce_{0.2}CuO_{4\pm\delta}$ in the present study is due to its nanocrystalline nature. In fact, the nanocrystalline material not only enhances the electrical conductivity, but also improves the electrode–electrolyte interface contact. Additionally, the surface to volume ratio increases, leading to increased surface area for catalytic activity. All these factors are responsible for the reduction in the ASR.

Conclusions

The sol–gel process yields nanocrystalline $Nd_{2-x}Ce_xCuO_{4\pm\delta}$ (x=0.1–0.2) solid solutions. The solid solubility limit of Ce in $Nd_{2-x}Ce_xCuO_{4\pm\delta}$ is found up to x=0.2. This is established by X-ray powder diffraction. The transition from negative temperature coefficient (NTC) to PTC, in sol–gel-derived samples, is observed at 620 °C. The maximum dc conductivity (σ=4.15 Scm^{-1}) is obtained for x=0.2. Oxygen partial pressure dependent ASR suggests good catalytic activity of $Nd_{1.8}Ce_{0.2}CuO_{4\pm\delta}$. The ASR value 0.93 ohm cm^2 at 700 °C, determined by electrochemical impedance spectroscopy (EIS) is comparable with 0.98 ohm cm^2 determined by V–I characteristics at the same temperature. The ASR of cell increases from 0.93 to 3.92 ohm cm^2 with increase in cell sintering temperatures from 800 to 1,200 °C. Such increase in ASR is due to increased grain size. Electrochemical performance and ASR of $Nd_{1.8}Ce_{0.2}CuO_{4\pm\delta}$ are improved when prepared by sol–gel route against solid-state reaction. This improvement is due to nanocrystalline grains being uniform size and shape. The ASR value 0.93 ohm cm^2 of $Nd_{1.8}Ce_{0.2}CuO_{4\pm\delta}$ prepared by sol–gel process compares better than those reported for other MIECs, which suggests that this may be a potential candidate as cathode for IT-SOFC applications.

Table 4 A comparison of ASR of cathode on GDC electrolyte using EIS and current–voltage measurements at different temperatures along with reported ASR from EIS for other MIECs

Cathode	T (°C)	ASR (ohm cm^2)		References
		EIS	Current–voltage	
$Nd_{1.8}Ce_{0.2}CuO_{4\pm\delta}$	500	183.03	197.8	[a]
$Nd_{1.8}Ce_{0.2}CuO_{4\pm\delta}$	600	10.23	11.39	[a]
$Nd_{1.8}Ce_{0.2}CuO_{4\pm\delta}$	700	0.93	0.98	[a]
$La_{1.6}Sr_{0.4}NiO_4$	700	3.06	–	[59]
$SmSrNiO_4$	700	3.06	–	[60]
$Nd_{1.6}Sr_{0.4}NiO_4$	700	0.93	–	[61]
$La_2Ni_{0.6}Cu_{0.4}O_{4+\delta}$	850	1.0		[24]

[a] Present study

References

1. Tsipis VE, Kharton VV (2008) J Solid State Electrochem 12:1367
2. Singhal SC (2002) Solid State Ionics 405:152–153
3. Yamamoto O (2000) Electrochim Acta 45:2423
4. Steele BCH (2001) J Mater Sci 36:1053
5. Huijsmans JP (2001) Curr Opin Solid State Mater Sci 5:317
6. Gorte RJ (2005) AIChE J 51:2377
7. De Bruijin F (2005) Green Chem 7:132
8. Kendall K (2005) Int Mater Rev 50:257
9. Sun C, Stimming U (2007) J Power Sources 171:247
10. Ullmann H, Trofimenko N, Tietz F, Stöver D, Ahmad-Khanlou A (2000) Solid State Ionics 138:79
11. Fukunaga H, Koyama M, Takahashi N, Wen C, Yamada K (2000) Solid State Ionics 132(3–4):279
12. Hibino T, Hashimoto A, Inoue T, Tokuno J, Yoshida S, Sano M (2000) Science 288(5473):2031
13. Jiang SP (2002) Solid State Ionics 146:1
14. Li SY, Lu Z, Wei B, Huang XQ, Miao JP, Liu ZG, Su WH (2008) J Alloys Compd 448:116
15. Steele BCH, Bae JM (1998) Solid State Ionics 106:255
16. Shao Z, Halle SM (2004) Nature 431:170
17. Liu QL, Khor KA, Chan SH (2006) J Power Sources 161:123
18. Kharton VV, Tsipis VE, Yaremchenko AA, Frade JR (2004) Solid State Ionics 166:327
19. Skinner SJ, Kilner JA (2000) Solid State Ionics 135:709
20. Daroukh MA, Vashook VV, Ullmann H, Tietz F, Arual Raj I (2003) Solid State Ionics 158:141
21. Wang YS, Nie HW, Wang SR, Wen TL, Guth U, Vashook VV (2006) Mater Lett 60:1174
22. Dong X, Wu Z, Chang X, Jin W, Xu N (2007) Ind Eng Chem Res 46:6910
23. Mehta A, Heaney PJ (1994) Phys Rev B 49:563
24. Aguadero A, Alonso JA, Escudero MJ, Daza L (2008) Solid State Ionics 179(11–12):393
25. Ding X, Kong X, Jiang J, Cui C (2009) J Hydrogen Energy 34:6869
26. Li Q, Zhao H, Huo LH, Sun L, Cheng X, Grenier JC (2007) Electrochem Commun 9:1508
27. Spinolo G, Scavini M, Ghigna P, Chiodelli G, Flor G (1995) Phys C 254:359
28. Soorie M, Skinner SJ (2006) Solid State Ionics 177:2081
29. Scribner Associates. Inc, (2003) Southern Pines, NC; www.Scribner.com
30. Holland TJB, Redfern SAT (1997) Mineral Mag 61:65
31. Voronin VI, Kar'kin AE, Goshchitski BN (1998) Phys Solid State 40(2):157
32. Kim JS, Kvam EP (1997) Phys C 292:203
33. Chaker H, Roisnel T, Potel M, Hassen B (2004) J Solid State Chem 177:4067
34. Scavini M, Chiodelli G, Spinolo G, Flor G (1994) Phys C 230:412
35. Radaelli PG, Jorgensen JD, Schultz AJ, Peng JL, Greene RL (1994) Phys Rev B 49:15323
36. Takagi H, Uchida S, Tokura Y (1989) Phys Rev Lett 62:1197
37. Khandale AP, Bhoga SS (2011) Solid State Ionics 182:82
38. Franceschetti DR, Macdonald JR (1991) J Electrochem Soc 138:1368
39. Hurt RL, Macdonald JR (1986) Solid State Ionics 20:111
40. Franceschetti DR, Macdonald JR (1979) J Electroanal Chem 100:583
41. Jonscher AK (1983) Dielectric relaxation in solids. Chelsea Dielectric Press, London
42. Gevers M (1946) Trans Farad Soc 42A:47
43. Macdonald JR, Brachman MK (1956) Rev Mod Phys 28:393
44. van Weppner W, Lenting BPM, Bijvank EJ, Hartog HW (1977) Phys Rev B16:2953
45. Ravaine D, Souqiet JL (1971) Phys Chem Glasses 18:27
46. Raistric RD, Ho C, Huggins RA (1976) J Electrochem Soc 123:1469
47. Roos A, Franceschetti DR (1984) Solid State Ionics 12:485
48. Bhoga SS, Singh K (2000) J Phys D Appl Phys 33:80
49. Raistrick ID, Franceschetti DR, Macdonald JR (2005) In: Barsoukov E, Macdonald JR (eds) Impedance Spectroscopy. Wiley, New Jersey, p 13
50. Raistrick ID (1986) Solid State Ionics 18/19:40
51. Raistrickand ID (1983) Solid State Ionics 9/10:425
52. Ho C, Raistrick ID, Huggins RA (1980) J Electrochem Soc 127(2):343
53. Thomas MGSR, Bruce PG, Goodenough JB (1985) J Electrochem Soc 132(7):1521
54. Singh K, Acharya SA, Bhoga SS (2006) Ionics 12:295
55. Salmon MB (ed) (1979) Physics of superionic conductors. Springer, Heidelberg
56. Khandale AP, Bhoga SS (2010) J Power Sources 195:7974
57. Mauvy F, Lalanne C, Bassat JM, Grenier JC, Zhao H, Dordor P, Stevens Ph (2005) J Eur Ceram Soc 25:2669
58. Murray EP, Barnett SA (2001) Solid State Ionics 143:265
59. Li Q, Fan Y, Zhao H, Huo LH (2006) Chin J Inorg Chem 22:2025
60. Li Q, Fan Y, Zhao H, Sun LP, Huo LH (2007) J Power Sources 167:64
61. Sun LP, Li Q, Zhao H, Huo LH, Grenier JC (2008) J Power Sources 183:43